NDT assessment of bonded assemblies - image optimization for weak bond characterization using ultrasonic array transducer

IOP Conf. Series: Journal of Physics: Conf. Series **1184** (2019) 012002 doi:10.1088/1742-6596/1184/1/012002

NDT assessment of bonded assemblies - image optimization for weak bond characterization using ultrasonic array transducer

Yasen Polihronov, Anthony Croxford

Department of Non-Destructive Testing, Department of Mechanical Engineering, Queen's Building, University Walk, Bristol BS8 1TR

E-mail: yp1504@my.bristol.ac.uk, A.J.Croxford@bristol.ac.uk

Abstract. Compromised interface bonds in structural components can lead to premature loss of structural integrity. Such defects are very difficult to detect using traditional acoustic inspection techniques. We assess the ability of linear ultrasonic Non-Destructive Testing (NDT) methods to detect or differentiate between weak-kissing bonds from healthy ones, by using a set of contaminated and non-contaminated bonds. An Ultrasonic Array Transducer (UAT) enables increased informational content, hence they have been used to detect and differentiate compromised bonds. Considerable research has been made into detecting weak bonds, but a practical, cost effective and industrially applicable solution remains elusive. The key problem is the signal changes are small, therefore we have developed an iterative testing methodology, in which the experimental variation in each of the following steps is significantly reduced: Sample Preparation; Data Acquisition; Imaging[1, 2]; Feature Analysis[3, 4]; Characterization/Classification; Interpretation. Our research addresses the issues related to UAT measurement techniques, specifically Full Matrix Capture (FMC)[1, 2] and Total Focusing Method (TFM)[1, 2], Scattering Matrix(derived) [3, 4] extraction in time domain, and other related or derived methods. Here the optimization of bondline imaging, resulting in higher quality and coherence of the imaging, is presented and discussed.

1. Introduction

1.1. Literature Review

The use of adhesives to bond components is becoming increasingly widespread, especially in aerospace and automotive industries. Despite some disadvantages such as cost and production issues (i.e. high curing pressure and temperatures)[5], bonding has the capacity to accommodate many benefits[6, 7, 8, 9, 10, 11] such as: reduced weight, increased stress dissipation, eliminating the need for riveting[12], thermal insulation, electrical insulation, resistance to corrosion (or specifically galvanic corrosion) which is of particular importance for corrosive environments. Other advantages, relative to traditional methods such as riveting or mechanical fastening, overcome the increased weight, cost and possibly production time limitations.

There is an ever-increasing need for more accurate Non-Destructive Testing (NDT) procedures for detecting weak-kissing bonds, particularly vital for applications in structural and high load components. In service or during production differentiating between various types of defects such as those, would enable rapid rectification and prevent future reoccurrence. The academic literature considers various interpretations of what a kissing bond (or extremely weak bond)

is[13, 14]. But for the purposes of this study, if a bond only contains a fraction of its intended strength, whatever geometry or mode of stress that may be in, then the extreme weakness (e.g. only 20% of its intended load bearing capacity) will be referred to as "kissing" or weak bond. A common method to induce this defect is by using contaminants on the bond[15], but this does not necessarily yield consistent results or imply (or guarantee) a kissing bond[16, 17, 18, 19]. Nevertheless, the contamination approach will be sufficient for this study. Various imaging and measurement methods have been tested for weak bond detection[6]. Broadly the methods can be categorized into linear and non-linear NDT methods. Among the linear methods, the most widespread approach utilizes normal incidence longitudinal waves, typically generated by a single monolithic probe. The effectiveness of normal incidence longitudinal waves to detect weak bonds has been assessed by several authors[20, 13, 21]. Their findings indicate that under higher contact pressure the defects are undetectable. To overcome this limitation higher frequency C-scans with sharp focus, as used by Nagy[20] and later by Vine[22], have been demonstrated to have increased sensitivity. Later work by Brotherhood[13, 21] indicates that this approach is viable, but has lower sensitivity compared to the non-linear modalities that were assessed. In particular, solid-solid contact kissing bonds were more sensitive to the variation in applied loading, in comparison to a liquid layer type of kissing bond.

Oblique incidence longitudinal wave and shear wave techniques have also found widespread industrial use in various applications. Typically, 2 or more transducers are inclined at equal and opposite angles for a transmit-receive configuration[23]. This type of NDT interrogation has been suggested to be one of the most promising in terms of sensitivity[23, 24, 25]. Proper alignment of the angles is of critical importance for the effectiveness of this approach, which is confirmed by a number of authors[22, 26, 24, 27, 20, 13, 21] who have examined the various modal options: the longitudinal-shear (LS) mode; shear-shear (SS); (SL) or the (LL) at an angle. Those modalities have been studied and results indicate that they have much higher sensitivity to weak bonds than normal incidence (LL) mode, however experimental challenges with positioning (critical angle) and coupling, could potentially be an issue in an industrial setting. Attempts have been made to achieve better coupling using EMATs[28, 21], however the lower signal to noise ratio leading to decreased sensitivity, could limit its industrial applicability.

Another significant approach to defect detection is Ultrasonic Spectroscopy, also referred to as Resonant Ultrasound Spectroscopy (RUS). It utilizes resonant frequencies and the effects of constructive/destructive interference based on the geometry of the joint[28]. This method involves measurement of shift or change of the (Gaussian) shape of the natural frequency due to energy transfer to harmonics after insonifying the structure using a wideband tone-burst(s)[29]. This approach is very susceptible to bondline thickness variation, resulting from manufacturing limitations, as opposed to defect induced changes in natural frequency due to the adhesive properties. Furthermore, it will not be suitable for thin samples, similar to the ones used in this study (see subsection 2.1).

Lamb waves have also been used to characterize bonding defects[28, 30, 31]. Here Lamb or Lamb-like waves are propagated along the surfaces or interfaces and thus velocity and wavelength are sensitive to boundary conditions[32], which is used to quantify the defect. Alternatively, they can be used to measure material properties related to the state of the bond[33, 30], such as attenuation, material velocity, material stiffness, reflection/transmission coefficients etc. They can also be used in combinations of modes and be guided, which allows for detection of volumetric defects along the bond. Tomography maybe need to produce an image using Lamb waves or guided waves, but in terms of imaging or visualization, arrays have the advantage as being able to image reliably faster, using smaller wavelengths, thus producing higher special resolution images. Furthermore, when Lamb/Lamb-like or shear waves propagated along the structure are used to measure the adhesive properties, the estimations will be averaged[34], whereas with arrays the measurements could be spatially localized.

Structural Health Monitoring (SHM) makes use of guided waves using Lamb-like modes or other types of modes, such as Shear wave (S-wave)/ horizontally polarized shear-wave (SH-waves)[35] modes. The difference here, is that reception and optionally emission equipment would almost always be embedded in the structure or permanently attached to it. This allows progressive monitoring over time and with a sufficiently distributed reception locations allows for imaging[36] using suitable algorithms (e.g. SAFT).

Other major approaches towards defect characterization include non-linear ultrasonic NDT methods[1, 37], which can be broadly categorized as into higher harmonic measurement (super harmonic), sub harmonic measurement, frequency mixing techniques and non-linear ultrasound spectroscopy. The general principle involves the generation of higher harmonics at higher input amplitudes. The non-linear response of the system, as the acoustic pulse passes through the bondline, is measured in terms of energy transfer from the base frequency to the higher or sub harmonics[1], absolute measurement of the amplitude of the harmonics or amplitude ratios, referred to as dimensionless non-linear parameters[37]. Those non-linear effects can be induced with all of the above-mentioned modalities at higher energy levels. Despite being potentially more sensitive, the reliable detection of the higher harmonics is difficult, as the non-linear effects could be very small in amplitude and thus overwhelmed by noise resulting from experimental variation. Nevertheless, linear methods are compatible with non-linear methods[1], which can potentially extend the testing procedure described in section 2.

Some other methods involving X-Ray based NDT[28, 5], shearographic/holographic inspection[5, 28] and novel methods for like Laser Ultrasonics[28, 38] are described in the literature, however they remain outside of the scope of this study.

1.2. Overview

Conventional NDT methods are not sufficiently sensitive to detect and differentiate bonding strength for regular use in industrial applications. Most of the research has been focused on single monolithic probes, where in most cases the authors would perform imaging and/or measurement of properties, but not classification or discrimination of the underlying data using classifiers on larger number of measurements. Phased Ultrasonic Array Transducer (UAT) based approaches provide more detailed information (FMC see section 2.2 & 2.4), potentially combining the benefits of incident wave and shear wave methods as well as non-linear array measurements. In UAT measurements the problem of coupling and angle alignment is overcome by the availability of multiple transducer elements at fixed optimized imaging distance. Therefore, the ability to input sound over a range of angles offers significant benefits, which could lead to possibly better testing performance.

The total Focussing Method (TFM) was selected as the imaging algorithm because a number of authors[3, 39, 40] indicate that it has superior imaging capability compared to a conventional C-scan. It should be noted that TFM is an UAT only algorithm, which naturally utilises the full amount of data available in the FMC. Therefore, a direct comparison may not be appropriate, as TFM and monolithic high-power probe imaging algorithms (such as B-scan/C-scan) differ categorically on number of criteria including: transducer power, number of elements N, focal lengthen, number of A-scans, number of A-scan contribution per pixel and other.

Bond characterization will be studied by classification of features extracted by a Scattering Matrix (SM) derived method (see 2.4). The TFM algorithm closely links with the SM methods, as both share the underlying focal law matrix which is used for amplitude extraction from FMC time-domain data (see 2.3 & 2.4). Historically these methods have been used for volumetric defects such as cracks[41], this could potentially explain disproportionate lack of weak bond detection attempts using TFM or SM in the literature. More studies are required for a better understanding of the true potential of UAT characterization and this study addresses the issue of reducing the experimental variation in the overall testing procedure in section 2, which is

done to potentially maximise the ability to detect kissing bonds. This study focuses on the optimization of the imaging step (i.e. 3^{rd} step in section 2) as the subsequent processing and classification are highly dependent on achieving accurate imaging localization. The subject of the optimization routine are the parameters necessary for generating the focal law matrix and the results from these optimization routines are presented in section 3.

2. Experimental Procedure - preparation, measurement and processing

Here we summarize the overall testing and processing chain, subsequently we discuss the individual applications and limitations. Using a generalized testing methodology allows us to validate a comprehensive approach by producing a small set of samples. This framework allows us to be flexible and develop the method in a generalizable way to accommodate potentially more complex testing scenarios. The generalized testing methodology is outlined in the following 6 steps:

Step 1: Manufacture 2.1 - preparation of a sample set of clean and contaminated bond samples
Step 2: Data Acquisition 2.2 - acquiring FMC in a consistent manner using immersion
Step 3: Imaging 2.3 - imaging the bondline using TFM
Step 4: Feature Analysis 2.4 - extraction of classification features using SM
Step 5: Characterization/Classification 2.5
Step 6: Interpretation 2.5 - generating consensus results from various classifiers

The 6 methodological steps outlined the general testing approach, this is illustrated in Figure 1. The benefits (see subsection 1.2) of data optimization techniques applied on defect imaging is highlighted in our result and discussion section 3.

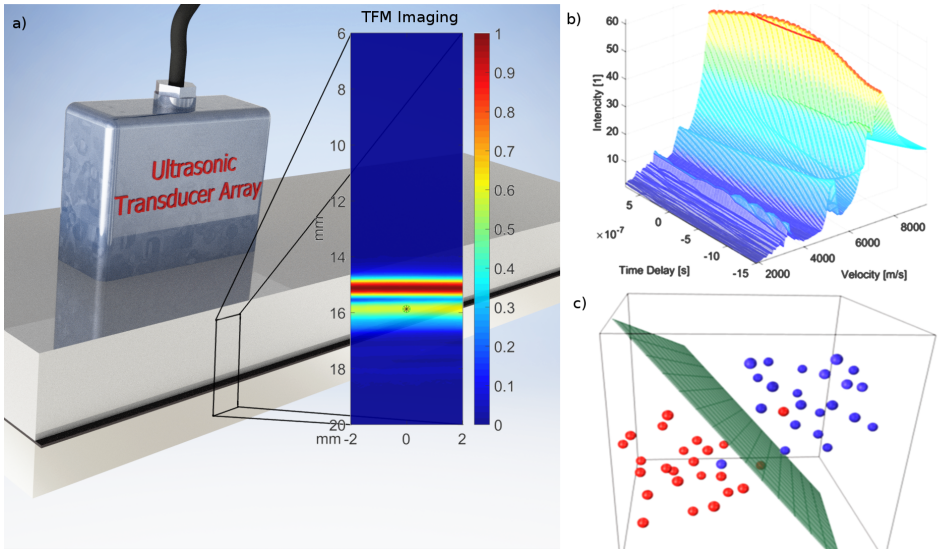

Figure 1: Methodology Visualized: a) Schematic representation of the experimental set-up with simple 2 layered sandwich structure. b) Imaging parameter optimization. c) Schematic of classified extracted scattering matrix(derived) features.

2.1. Step 1: Sample Preparation

Two single layered aluminium plates as shown in Figure 1 a) and Figure 2 are bonded in a sandwich structure with Araldite Huntsman 2014 - 2-part epoxy adhesive. Separators were used at the edges of the bond to ensure consistent bond thickness of 0.325mm along the length of the sample. An additional layer ($< 100\mu$m) of Castrol Care Cut ES1 lubricating oil was used as a

contaminant on half of the samples. The sample set includes 4 samples in total, with adhesive thickness of 0.3mm, which aims to match a more realistic bondline condition as used in actual industrial applications. A simple design is easy to assemble consistently. The premise is that quality examination of a simple case will assess the capability of the methodology, which could be adapted for more complex bond scenarios in the future.

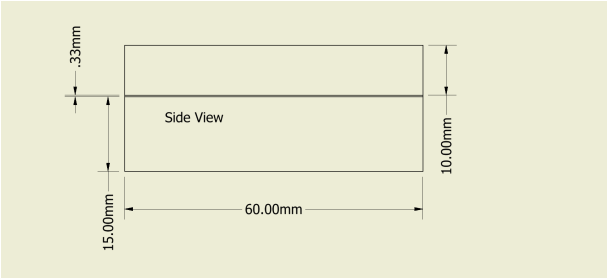

Figure 2: Sample side view schematic of the sample

2.2. Step 2: Data Acquisition

A 5Mhz 64 Element Imasonic UAT with PeakNDT MicroPulseFMC array controller was used for data acquisition. The Full Matrix Capture (FMC)[1, 2] was acquired at 200Volts, with a 100MHz sampling frequency and with 16bits depth quantization resolution. The hardware amplification of the reception signal is at +19dB gain. The acquisition settings are constant throughout the acquisition process for all FMC frames. The values are set such that the highest signal to noise ratio is achieved without signal distortion throughout all FMC frames.
Initially the acquisition was performed by hand using a water-based gel Sonagel from Sonatest for coupling between the UAT surface and the sample's surface, but this approach did not yield consistent coupling results due to coupling variation, inconsistent pressure and gel sticking. Consistent coupling was achieved (see gain profile in Figure 3) by using a manual array positioning assembly (see Figure 4), where the sample and the array are immersed in a water bath and both surfaces were in contact.

2.3. Step 3: Imaging

The first stage of the data analysis here is imaging the bondline. This includes accurate determination of the position and thickness of the bondline separating the two aluminium plates. Imaging through TFM[1, 2] (also 1.2) requires a focal law vector to be computed for any given pixel. The focal laws determine the precise contribution from each A-scan in the FMC for a given pixel as shown in Equation 1.

$$I(\mathbf{r}) = \sum_{i,j \in E} g_{(i,j)} \left(t_{(i,j)} = \left[\frac{1}{v} (\mathbf{d_i}(\mathbf{r}) + \mathbf{d_j}(\mathbf{r})) \right] + t_d \right) \tag{1}$$

where I is the pixel intensity, located at position vector $\mathbf{r}$. $\mathbf{d_i}$ and $\mathbf{d_j}$ are the distances defined by the vector paths from transmit element i to point $\mathbf{r}$ and respectively receive element j to $\mathbf{r}$. The TFM algorithm in Equation 1 sums all contributions from transmit-receive pairs i, j for all elements $E \equiv [1 : N]$, where $N = 64$. The contribution from A-scan $g_{(i,j)}$ from the full FMC, is determined by the correct focal law time $t_{(i,j)}$ based on the (signal) ray path from the location of elements i, j and position vector $\mathbf{r}$, and the velocity of sound in the medium v. Using all combinations of i, j, all $t_{(i,j)}$ values can be arranged into vector or matrix form, which we also

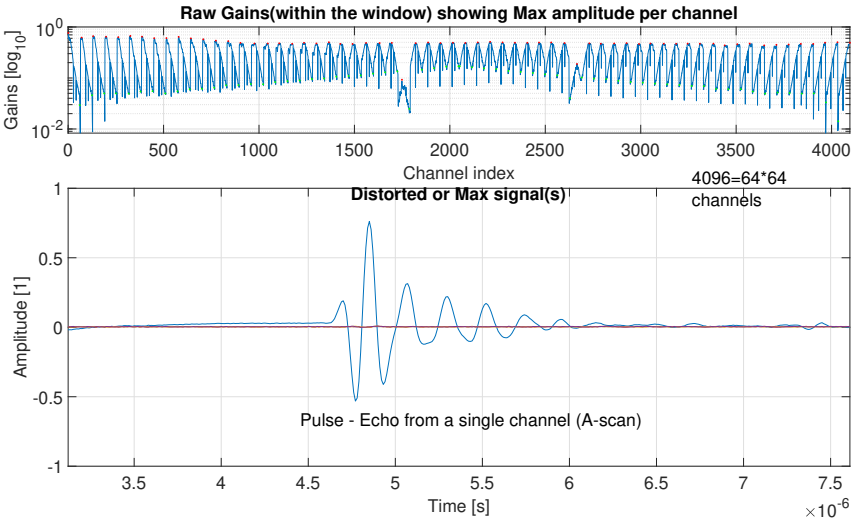

Figure 3: The logarithmic raw FMC gains (top plot) shows the acquisition gain profile for a single FMC test, where the line shows the maximum amplitude per channel. The highlighted in red top points represent the transmit and receive pair for the same element and indicate approximately uniform gain and coupling profile. Gain refers to the raw signal level as received by the array controller. "Amplitude" is the is a normalized voltage from $[-1$ to $1]$. A single A-scan from the FMC is shown on the bottom plot. The highest peak indicates the reflection from the interface between the inner back-wall and top of the bondline.

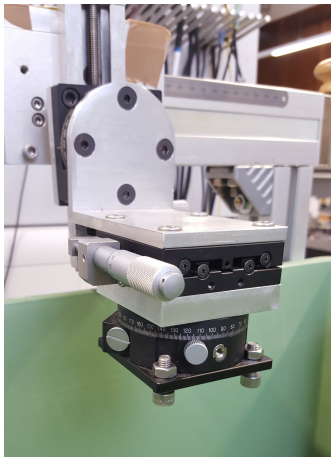

Figure 4: The image shows the UAT holder used for immersion contract acquisition.

refer to as the focal laws (law matrix). t_d is the time-delay parameter that we aim to optimize along with the velocity of the medium v.
As mentioned in subsection 1.2, the focus of this paper is the optimization of this step, which outlines the focal laws $t_{(i,j)}$ and the parameters involved in the optimization procedure t_d and v. The optimization is needed to compensate for varying coupling conditions or fixed discrepancies. t_d and v can be adjusted in order to produce images that better represent the internal sample geometry. The time delay parameter t_d compounds all sources of electromechanical delay and accounts for the adjustment needed to determine exactly when the acoustic pressure front enters into the medium with the prescribed velocity v. The electronics of the array controller and the characteristics of the transducer array are responsible for the fixed component of t_d, which should be constant and consistent between FMC acquisitions. The variable part of the compound time delay refers to the variation in coupling conditions (i.e water/gel layer thickness) and potentially significant surface roughness, discussed in subsection 2.2. Additionally, it is noted that t_d is an average measure, for all transducer array elements, accounting for the previously described effects.

2.4. Step 4: Feature Analysis & Feature Extraction

Various types of processing are applied to prepare the raw FMC data into a classifiable feature set, which is necessary in order to approach the bond characterization as a machine learning challenge. Starting with the acquisition, the FMC sets are imaged and localization of points of interest is accomplished through TFM. Features from those points are extracted for classification as amplitude and phase through the Scattering Matrix (SM)-derived method [3, 4] in the time domain. The method would extract the scattering amplitudes at given focal locations and

thus form a normalized matrix of reflection coefficients of longitudinal waves at various angles. Various levels of energy loss, due to shear wave mode conversion, is expected to be encoded depending on the condition of the bondline. An example of such a scattering matrix can be found in Fig.2 in [4]. Although not used here, Principle Component Analysis (PCA) is a technique that could be used for dimensionality reduction[4].

Here we outline the main concepts of the feature extraction routine, further details will be presented in future publications as it is not the focus of the current study. Three specific bond TFM locations are used to describe the feature space: bond top interface, bond middle, and bond bottom interface. Those locations are visualized in figures 5a & 5b, midpoint of top(red) line, between top(red) and bottom(yellow) lines and middle of yellow line respectively represent the three locations formerly outlined.

The most informative features for characterization can be selected using the Fischer criterion given in Equation 2. It is computationally efficient to test different processing options, as well as to determine optimal location for feature extraction to be used. Also known as Fischer Discriminant Ration, it quantifies the discrimination between any two feature sets, thus measures the separability of any given batch of feature data before actual classification. For the purpose of this study, the ratio is used to determine if the optimization improves the overall separability of the feature sets between the different samples.

$$F = (m_1 - m_2)^2/(s_1^2 + s_2^2) \tag{2}$$

Where "m" represents the means of any two feature sets indexed 1 and 2. "s" represents the within cluster variance of a feature set. Each feature within the set is the vectorized scattering matrix, as noted earlier, additional processing could be used if relevant. The aim is to optimize all processes such that the Fisher ratio "F" is maximized. The optimized imaging should reduce the experimental variation, hence as the denominator of Equation 2 becomes smaller, "F" will increase along with the discriminative capability of the better localized feature set. When the feature space is smaller it is important to have a greater criterion value, such as $F > 2$, in the original or processed (e.g. PCA) space. With larger feature spaces a lower F value would be acceptable for most features, if there is at least one pair allowing for highly descriptive feature clustering or some of the features individually have higher fisher criterion.

2.5. Step 5: Characterization Classification

Once the data is sufficiently discriminative it is relatively straight forward to test simple classification routines, as there are various types of classifiers available for different kinds of data sets[42]: Linear Classifiers including Logistic Regression or Naive Bayes Classifier, non-linear regression or high dimension separation surfaces Support Vector Machines, Decision Trees, Neural Networks, Nearest Neighbour, k-means clustering and others. Currently only a linear classifier is used for classification, due to the generally high dimensional space of N^2, where the number of array elements is $N = 64$. The use of simple classifier along with high fisher ratio, should ensure that the classification results are much less likely to be misinterpreted or incorrectly used. With $N^2 = 4096$ features in the original classification feature space the classifier is highly under-determined (under-constraint). Vector distance away references metric, in this case the testing set means, has been used as the simplest feature reduction option. Also, PCA transformation or sub-aperture averaging are some of the options that have been explored, however the classification results have been found to be higher in the original full feature space with a specific set of testing parameters. This is likely due to the higher fisher criterion by small number individual features.

The 6^{th} and final step involves the interpretation of the classification results and the combination of different classifiers or locations to assess the consensus state of the bondline both qualitatively and quantitatively.

3. Results & Discussion

The TFM was used to image the bondline in the experimental sample. The imaging was done at the same central location for the bondline for sample 1 as shown in 5a & 5b from the 15mm and 10mm layer sides respectively.

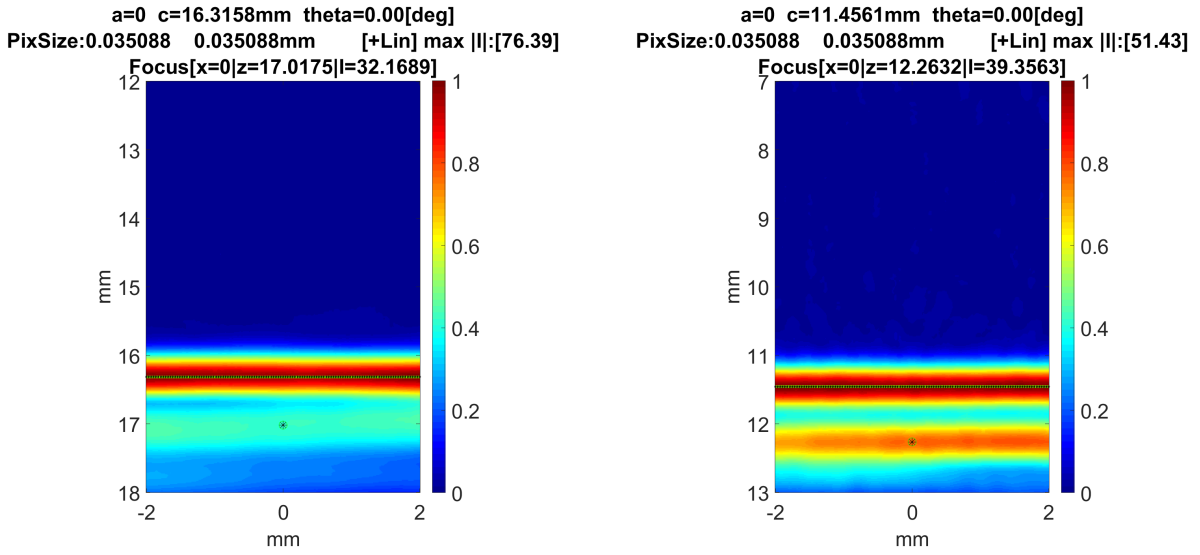

(a) TFM image of the bondline from the 15mm layer.

(b) TFM image of the bondline from the 10mm layer.

Figure 5: For both images the velocity of Aluminium $v = 6300$m/s and the time delay $t_d = 0$. The green dotted line shows the estimated incline of the imaged bondline where **a,c,theta** are the gradient, intercept and angle respectively. The star(focus) below the incline line shows the peak of the bottom of the adhesive layer. **[+Lin]max|I|** indicates the maximum value of the linear scale and the colour-bar indicates the percentage of the intensity.

The figures show significant difference between the actual and the imaged location of the bondline. The 15mm line is imaged at 16.32mm resulting in 1.32mm (8.8%) error. The 10mm line is imaged at 11.46mm resulting in 1.46mm (14.6%) error, which may lead to inaccurate localization and feature extraction.

To compensate for this discrepancy in the image the focal laws have been used to account for additional delays and errors such as: possible time delay in the equipment, time of flight in the coupling layer and uncertainty in the material dependent acoustic velocity. Uniform gain profile, as discussed in subsection 2.2, should provide a consistent FMC, however there is not an exact method for computing the thickness of the coupling interface or the effects of the pressure between the array and the sample surface. We suspect that the water coupling interface layer has significant influence on the time delay parameter. Water has a velocity of 1450-1498m/s at room temperatures 20°C to 25°C, which is just over 4 times slower than the velocity of sound in aluminium. Time taken for receiving the first reflection is typically used to measure the thickness of the water layer in immersion testing when there is distance between the sample and the array surface, however in our case the water layer is too thin for this approach to be viable. The signal self-interference (cross-talk) prevents reflections from sources immediately next to the array surface being accurately isolated. Since TFM(Equation 1) sums the contribution from a large number of A-scans, accurate focal laws should focus the image, maximize the localization accuracy and reduce the point spread of the interface. The parameters that we optimize for are the velocity v and the time-delay t_d. There are other types of optimizations that are discussed

by Hunter[3], where the interface is curved or flat at an angle. Here we assume the surface of the sample is flat, although the optimization should be viable for non-flat surfaces as well. A small imaging tilt (> 0.60 deg) has been observed in some of the experiments, however with careful alignment of the array coupling and uniform gain profile, the tilt is mostly corrected for during the data acquisition stage.

3.1. Optimization cost function, parameter space and optimization routine

The optimization of the $t_{i,j}$ focal laws (Equation 1) is accomplished using a region of interest in which the artefacts of interest are expected to be found (e.g. the adhesive layer imaged in figures 5a,5b,8a & 8b). Generally, the two fundamental components in any optimization routine are method and criterion. Here the method is to minimize a criterion, which is shown by the cost function in Equation 3.

$$f(t_d, v) = -\max(process_n(tfm(FMC, focalLaws(t_d, v, FMC), \underline{R}, \mathbf{S}))) \tag{3}$$

where $f(t_d, v)$ is the minimization (cost) function, which is optimized for a given experimental FMC data set as described in subsection 2.2. The $focalLaws()$ function computes the focal law matrix $t_{i,j}$, based on the input time delay t_d, the input speed of sound in the material v and the FMC(Equation 1). The $process_n()$ uses the full TFM image data to process the TFM or extract the profile within the region of interest, denoted by the coordinate matrix $\underline{R}$. The $\mathbf{S}$ structure(matrix) denotes all additional settings and parameters necessary for the imaging algorithm, in this case the pixel size being the most important additional parameter.
The $process_n()$ output is an image matrix, the maximum value is extracted through max() and the negative sign reflects the function to ensure minimization can be applied to the cost function. The optimization space is explored for one of the samples as shown in 6a and 6b.

The optimization of Equation 3 can be achieved through the use of Newton-Raphson

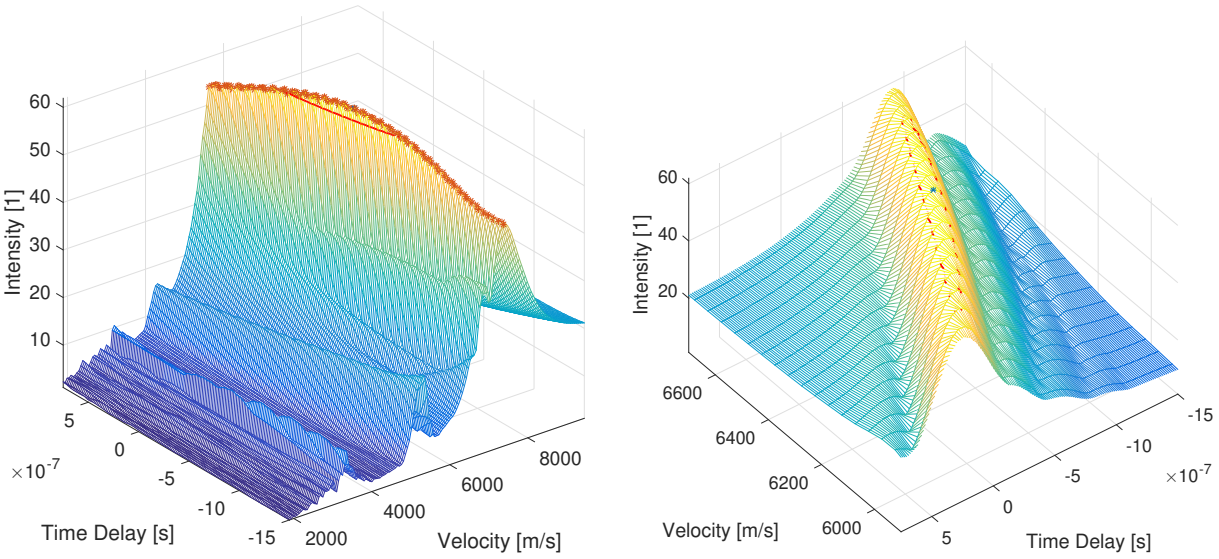

(a) Orientation 1 (b) Orientation 2

Figure 6: Shows the parameter space and the value of the highest(max/mean) intensity. 6b shows close up view of 6a along different orientation.

optimization scheme. However closer inspection of the cost function shown in Figure 7,

reveals that cost function roughness will cause the optimization algorithm to get stuck into a sub-optimum minimum. To address this issue the Newton-Raphson has been coupled with GA(Genetic Algorithm) sequentially. First the GA attempts to get close to the maximum and

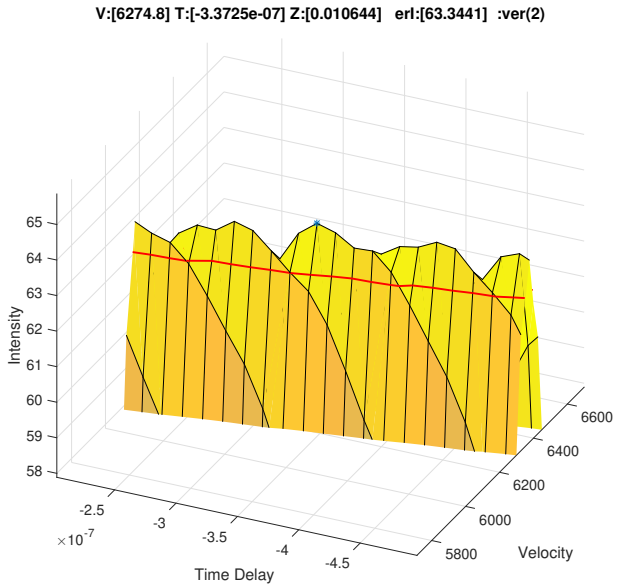

Figure 7: Close up view around the apex(maximum) of 6a & 6b, showing the uneven parameter space surface.

after a particular threshold is reached the algorithm switches to Newton-Raphson. Without sweeping the 2-dimensional input space for $f(t_d, v)$ with every FMC, it cannot be guaranteed with absolute certainty if the algorithm has indeed reached the optimum minima. It is not computationally efficient nor practically viable to compute the full(bounded) input parameter space, neither is it practical to optimize every FMC in real time imaging as it is computationally intensive process. The algorithm can be made more efficient for real time optimization, but presently, the post processing analysis confirms the direct measurements.

3.2. Results of the parameter optimization routine

8a & 8b show the optimized bondline image, computed with the default parameter values given in figures 5a & 5b. The figures show much smaller discrepancy between the actual and the imaged location of the bondline. The 15mm line is imaged at 15.16mm resulting in 0.16mm (1.1%) error, while the 10mm line is imaged at 10.30mm resulting in 0.30mm (3.0%) error. This is a reduction of 8.33 and 4.88 times in localization error respectively. These results indicate that the optimization with the common parameter set is sufficient and there is only marginal benefit to optimizing each individual FMC.

Each experimental sample was imaged at 5 mm intervals and the results from the analysed data are summarized in 9a & 9b, where the maximum intensity within the region of interest $\underline{R}$ imaged with the default and the optimized values, are shown.

The optimization values for each individual FMC are shown in figures 10b & 10a, where the velocity fluctuates around 6322m/s with average standard deviation of 49m/s. The results from 10b show that without prior constraints the algorithm converges the velocity to the expected value, which is the default aluminium velocity of 6300m/s. The results also appear to be consistent from sample to sample, as the time delays from the different samples have

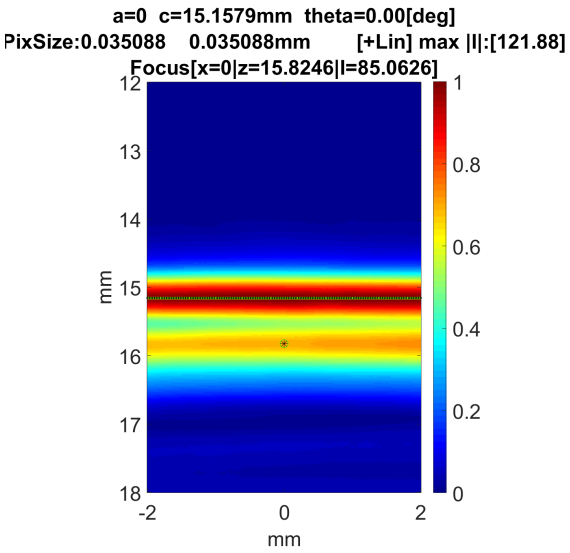

(a) Shows the sample imaged from the 15mm side (sample layer).

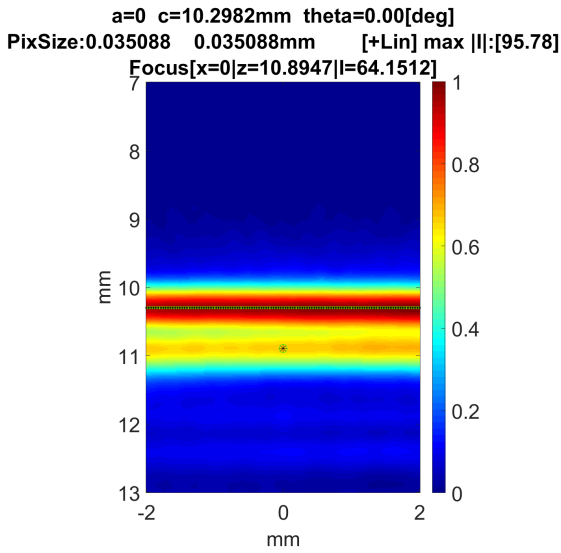

(b) The same sample imaged from the 10mm side (sample layer).

Figure 8: Velocity of Aluminium $v = 6300$m/s and the time delay $t_d = 3.79e-7$s. Other plot features explained in figures 5a & 5b.

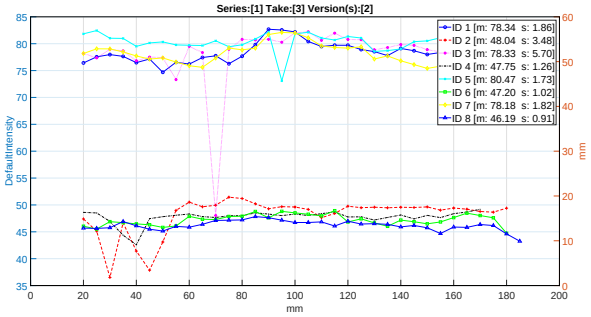

(a) Samples' intensity with default values. $t_d = 0$s.

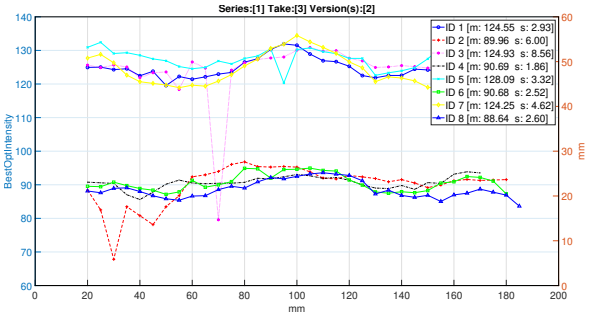

(b) Samples' intensity with optimized values. $t_d = 3.79e-7$s

Figure 9: Shows the intensity values of the samples with default values in 9a & optimized values in 9b. The velocity of Aluminium in both cases is $v = 6300$m/s. Here and throughout this study, the "ID" labelling identifies the sample surfaces. The odd indices represent the 15mm layer surfaces of the samples and the adjacent even indices represent 10mm layer surfaces. For example, the second sample block is indexed by "ID 3" for the 15mm side and "ID 4" for the 10mm side.

approximately the same means and standard deviations, as shown in 10a.

We can address the computational applicability of the optimization by performing the optimization in preprocessing and selecting average common values. Thus, for simplicity the common optimization velocity remained 6300m/s and the common time-delay is $3.79e-07$s. 11a & 11b show the comparison of the intensity increase in two distinct cases. The difference in 11a between non-optimized verses the common v & t_d optimization set is quite significant. The 10mm point shows $50-60\%$ increase, while the 15mm point shows $90-100\%$ increase, from

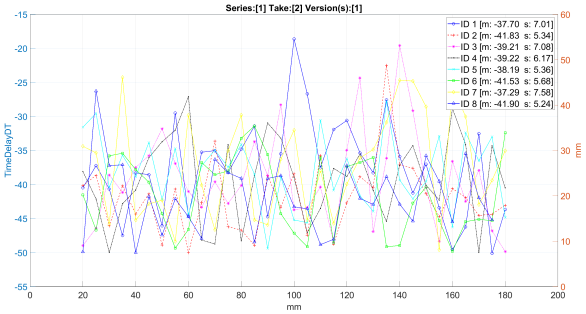

(a) Optimized Time Delay, y-axis in $dt = 10^{-8}$ units of 100HMz

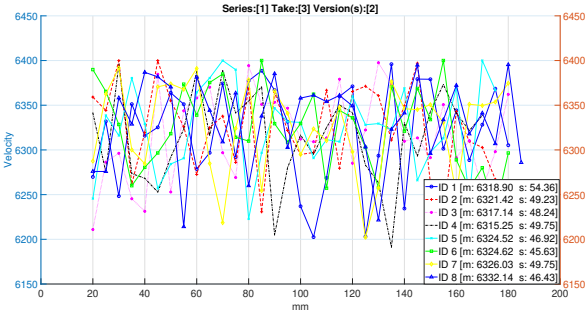

(b) Optimized Velocity

Figure 10: Here and throughout this study, the 8 lines represent the 4 samples imaged for each surface. The even numbered "ID"s represent the 110mm sides, the odd numbered "ID"s represent the 15mm sides.

which we conclude the optimization has more significant focusing effect on the points that are farther from the array contact. This is in line with the fact that as the ultrasonic pressure wave spreads, the power decreases with the inverse square of the distance travelled, such that points that are farther are more affected by misalignment resulting in larger point-spread. The increase from the common parameter set optimization to the individual set in 11b is only marginal from $0-2\%$ to $1.5-4\%$ for the 10mm and 15mm case respectively

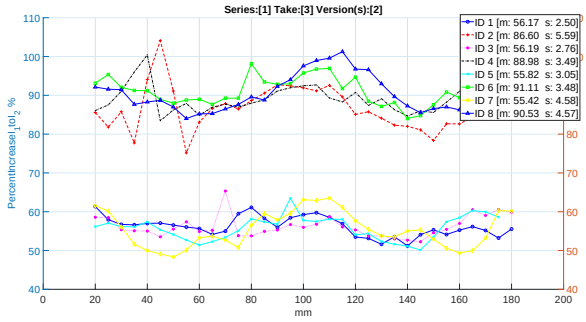

(a) The common set optimization case against the non-optimized with default parameters.

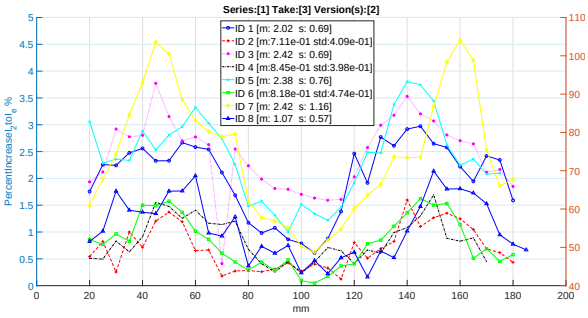

(b) The maximum optimization with individual parameter set for each FMC against the optimized case with common parameter set.

Figure 11: The plot shows the percentage increase in intensity

The localizations for the default case are given in 12a, which shows significant adhesive location offset with relatively small variation from sample to sample. In the optimized case, the variance of the localization is much greater, however the adhesive is imaged much more closely to its true location as shown in 12b. Therefore, these results validate the effectiveness of this optimization strategy, by showing clear improvement in the intensity and localization of the adhesive layer.

3.3. Optimization influence on Fisher Criterion

As discussed in subsection 2.4, here we only assess the effect of the optimization routine on the separability of the data. Contrary to initial expectation in both cases after optimization the separability appears to decrease slightly. Despite the better localization and the increase in

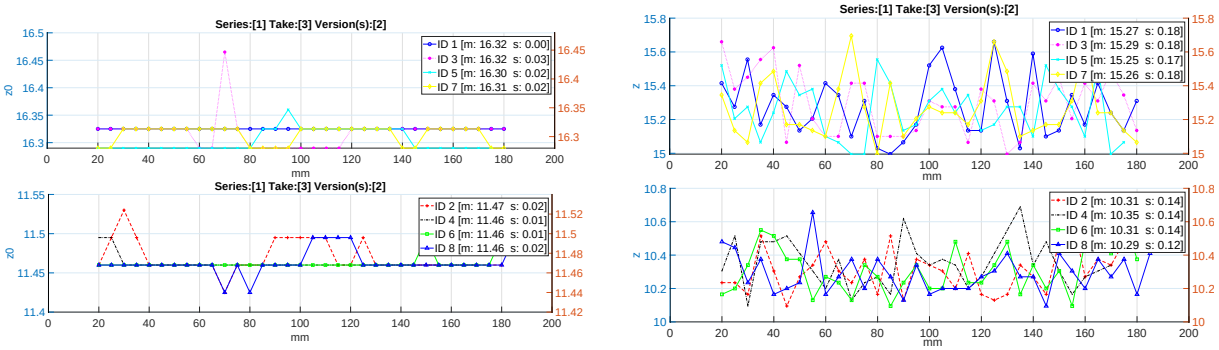

(a) Z-Coordinates Unoptimized (b) Z-Coordinates Optimized

Figure 12: The plot shows the bondline position from both sides for the optimized and non-optimized case

intensity as shown in subsection 3.2, the variance in both location and intensity of the features is greater, which is in line with the results shown in figures 13a,13b,14a and 14b. Another interesting observation is that the features from 15mm side have proportionately lower average Fisher ratio, than the 10mm side. One possible explanation is the fact that closer points allow the array higher angular span, while points farther away have lower angular span. Furthermore, the contaminant was applied on the 10mm side, therefore extracting data directly from the contaminated side potentially explains the higher discrimination. Regardless of the decrease in

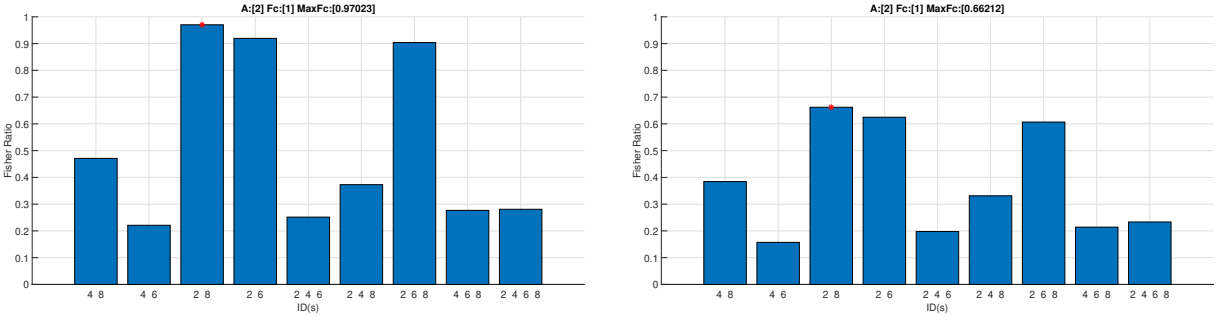

(a) Non-Optimized Fisher criterion. (b) Optimized Fisher criterion.

Figure 13: The graphs show the mean fisher criterion of the feature vectors from the 10mm side. The x-axis shows all valid training combinations. The features presented here are from the first extraction location as given in subsection 2.4.

the average Fisher ratio, the results shown in figures 13a to 14b also reaffirm our supposition of the importance of accurate localization. In addition to the effects of the increased variance, it is also possible that the fisher criterion has been falsely inflated due to the incorrect localization, thus implying that optimized results are true(truer) while the non-optimized are not reliable.

4. Conclusion

Imaging optimization has been performed on bonded assemblies. The optimization routines have successfully improved the image focusing by increased coherence of the FMC by adjusting the material velocity and the time delay. The improved focusing has resulted in better localization

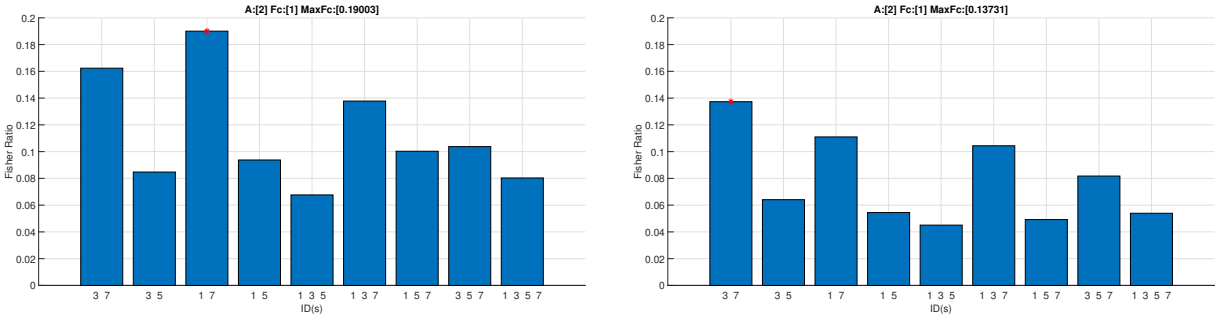

(a) Fisher criterion Non-optimized Odd IDs

(b) Fisher criterion Optimized Odd IDs

Figure 14: The graphs show the mean fisher criterion of the feature vectors from the 15mm side. The x-axis shows all valid training combinations. The features presented here are from the first extraction location as given in subsection 2.4.

and constructive interference leading to reduced point spread of the scatterers.
The effect of the optimization on the classification is not conclusive as it appears there is a trade-off between the increase in variance and decrease in localization error. More studies with potentially larger sample sets are needed to assess this more accurately.
The auto focusing requires minimal-to-no prior knowledge about the actual magnitude of the optimization parameters. This technique could be robustly applied for cases were the exact material properties or geometry are not known. The technique is also robust to variance in the coupling conditions, although it is not exactly known if the former variance relates directly to the variance of the optimized parameters. Accurate imaging is particularly important for the subsequent localization, scattering matrix extraction and classification. Depending on imaging distance, up to 120% improvement in imaging coherence has been observed.

4.1. Challenges

Bondline variability has been observed in the cross-sectional acoustic images of the samples (along the length of the samples), which is attributed to the material properties of the adhesive and the geometry of the sample. It is possible that this acoustically observed variation is the cause of the optimized parameter set variance. A possible strategy to test the exact cause for the time-delay is to run imaging optimization on the same sample using different thin-layer coupling mediums and assess their effect on the focusing within the sample. A statistical distribution of FMC sets taken at the same location, can help determine the extent of this uncertainty. The results could also be compared with other forms of NDT such as X-ray, to determine whether there is indeed variation in the bondline thickness.

4.2. Future Work

A number of challenges have to be overcome before the method presented in this work can be fully utilized for weak bond assessment. The initial results have encouraged further exploration of the versatility and the ability to test various materials, therefore the aspect of classification output will be presented in future publications. Automation of this approach would be of particular interest to the automotive and aerospace industries during production, post-sale equipment maintenance and in-service testing. Also, fully automating the data acquisition process will be necessary for the positioning, surface alignment and coupling, due to the large amount of FMC data that is required for accurate classification or imaging. This approach could result in increased quality assurance of the bonded assemblies in a robust and reliable way. The other

aspects of this approach, such as thin layer optimization incorporating multi-layer refraction in the focal laws, improvements and research outcomes, will be discussed in future publications. Ongoing work focuses on further improving the localisation of points of interest, in a multilayer structure through a robust automatic process. We hope this will further increase the separability of the classification data. Finally, another potential strategy worth investigating in a future study, that could reduce the experimental variation in the optimization set output, would be to use constant thickness film adhesives.

References

[1] Potter J N, Croxford A J and Wilcox P D 2014 *Physical Review Letters* **113** 144301 ISSN 0031-9007 URL https://link.aps.org/doi/10.1103/PhysRevLett.113.144301
[2] J Zhang and B W Drinkwater and P D Wilcox 2013 *IEEE Transactions on Ultrasonics, Ferroelectrics, and Frequency Control* **60** 1732–1745 ISSN 08853010
[3] Hunter A J, Drinkwater B W and Wilcox P D 2010 *NDT and E International* **43** 78–85 ISSN 09638695 URL http://dx.doi.org/10.1016/j.ndteint.2009.09.001
[4] Bai L, Velichko A and Drinkwater B W 2015 *IEEE Transactions on Ultrasonics, Ferroelectrics, and Frequency Control* **62** 545–559 ISSN 08853010
[5] Bowen R L, Eichmiller F C, Marjenhoff W a and Rupp N W 1989 *The Journal of the American College of Dentists* **56** 10–13 ISSN 0002-7979
[6] G M Light H K 1989 Nondestructive Evaluation Of Adhesive Bond Quality Tech. Rep. June Southwest Research Institute - Nondestructive Testing Information Analysis Center San Antonio, Texas
[7] Charla K 2001 *Composite Materials Science and Technology* (Springer, New York (EEUU))
[8] Rastogi N 2004 *SAE Technical Paper* (SAE International) URL http://dx.doi.org/10.4271/2004-01-0485
[9] Choi J H 1997 *Composite Structures* **38** 309–319 ISSN 02638223
[10] Arenas J M, Alía C, Narbón J J, Ocaña R and Recio M M 2012 **498** 67–72 ISSN 10226680
[11] Patil D D, Shinde R M and Sawant S M 2016 **6** 1532–1536
[12] Schjive J 2003 *International Journal of Fatigue* **25** 679–702 URL http://www.springerlink.com/content/h1245730r0283vrl/
[13] Brotherhood C J, Drinkwater B W and Guild F J 2002 *Journal of Nondestructive Evaluation* **21** 95–104 ISSN 1573-4862 URL http://dx.doi.org/10.1023/A:1022584822730
[14] Jiao D and Rose J 1991 *Journal of Adhesion Science and* **5** 631–646 ISSN 15685616
[15] Jeenjitkaew C, Luklinska Z and Guild F *International Journal of Adhesion and Adhesives* 643–653 ISSN 01437496 URL http://dx.doi.org/10.1016/j.ijadhadh.2010.06.005
[16] G Hong S and X Shu H 1994 *Journal of Polymer Science Part B: Polymer Physics* **32** 2421–2433
[17] Debski M, Shanahan M and Schultz J 1986 *International Journal of Adhesion and Adhesives* **6** 145–149 ISSN 01437496 URL http://linkinghub.elsevier.com/retrieve/pii/0143749686900175
[18] Debski M, Shanahan M E R and Schultz J 1986 *International Journal of Adhesion and Adhesives* **6** 150–152 ISSN 01437496 URL http://linkinghub.elsevier.com/retrieve/pii/0143749686900187
[19] Greiveldinger M, Shanahan M E R, Jacquet D and Verchère D 2000 *The Journal of Adhesion* **73** 179–195 ISSN 0021-8464 URL http://www.tandfonline.com/doi/abs/10.1080/00218460008029305
[20] Nagy P B 1991 *Journal of Adhesion Science and Technology* **5** 619–630 ISSN 0169-4243 URL https://doi.org/10.1163/156856191X00521
[21] Brotherhood C J, Drinkwater B W, Guild F J and Building Q 2003 **22** 1033–1040 ISSN 0094243X
[22] Vine K, Cawley P and aJ Kinloch 2002 *NDT & E International* **35** 241–253 ISSN 09638695
[23] Vine K, Cawley P and Kinloch A J 2001 *The Journal of Adhesion* **77** 125–161 ISSN 0021-8464 URL https://doi.org/10.1080/00218460108030735
[24] Pilarski A and Rose J L 1988 *NDT International* **21** 241–246 ISSN 03089126
[25] Vijaya Kumar R L, Bhat M R and Murthy C R L 2013 *Ultrasonics* **53** 1150–1162 ISSN 0041624X URL http://dx.doi.org/10.1016/j.ultras.2013.01.014
[26] Rose J L, Dale J, Ngoc T D K and Balasubramaniam K 1990 *Review of Progress in Quantitative Nondestructive Evaluation* **9** 1309–1316 URL https://doi.org/10.1007/978-1-4684-5772-8_168
[27] Jiao D and Rose J 1991 *Journal of Adhesion Science and* **5** 631–646 ISSN 15685616 URL http://www.tandfonline.com/doi/abs/10.1163/156856191X00530
[28] Adams R and Drinkwater B 1997 *NDT & E International* **30** 93–98 ISSN 09638695 URL http://linkinghub.elsevier.com/retrieve/pii/S0963869596000503
[29] Zou X, Schmitt T, Perloff D, Wu N, Yu T Y and Wang X *Measurement: Journal of the International Measurement Confederation* 74–80 ISSN 02632241 URL http://linkinghub.elsevier.com/retrieve/pii/S0263224114005399

[30] Challis R, Bork U and Todd P *Ultrasonics* 455–459 ISSN 0041624X URL http://linkinghub.elsevier.com/retrieve/pii/0041624X9500115J
[31] Lowe M J S, Cawley P, Kao J Y and Diligent O *The Journal of the Acoustical Society of America* 2612–2622 ISSN 0001-4966 URL https://doi.org/10.1121/1.1512702
[32] Castaings M and Hosten B 2003 *The Journal of the Acoustical Society of America* **113** 2622–2634 ISSN 0001-4966 URL http://asa.scitation.org/doi/10.1121/1.1562913
[33] Drinkwater B W, Castaings M and Hosten B *The Journal of the Acoustical Society of America* 3161–3170 ISSN 00014966 URL https://asa.scitation.org/doi/abs/10.1121/1.1568754
[34] Mezil S, Bruno F, Raetz S, Laurent J, Royer D and Prada C ISSN 0001-4966 (*Preprint* 1511.04367) URL http://dx.doi.org/10.1121/1.4934958
[35] Castaings M 2010 *10ème Congrès Français d'Acoustique* 12–16
[36] Yu X, Fan Z, Puliyakote S and Castaings M 2018 *Smart Materials and Structures* **27** ISSN 1361665X
[37] Yan D, Drinkwater B W and Neild S A 2010 *AIP Conference Proceedings* **1211** 1190–1197 ISSN 0094243X
[38] Ehrhart B, Ecault R, Touchard F, Boustie M, Berthe L, Bockenheimer C and Valeske B 2014 *International Journal of Adhesion and Adhesives* **52** 57–65 ISSN 01437496 URL http://linkinghub.elsevier.com/retrieve/pii/S0143749614000918
[39] Nanekar P, Kumar A and Jayakumar T *Case Studies in Nondestructive Testing and Evaluation* 9–14 ISSN 22146571 URL http://linkinghub.elsevier.com/retrieve/pii/S2214657115000027
[40] Zhang J, Drinkwater B W, Wilcox P D and Hunter A J 2010 *NDT and E International* **43** 123–133 ISSN 09638695 URL http://dx.doi.org/10.1016/j.ndteint.2009.10.001
[41] Cheng J, Potter J N, Croxford A J and Drinkwater B W 2017 *Smart Materials and Structures* **26** 055006 ISSN 0964-1726 URL http://stacks.iop.org/0964-1726/26/i=5/a=055006?key=crossref.20e84e887a58c9df070dd2465d59319b
[42] Wu X, Kumar V, Ross Quinlan J, Ghosh J, Yang Q, Motoda H, McLachlan G J, Ng A, Liu B, Yu P S, Zhou Z H H, Steinbach M, Hand D J, Steinberg D, Ross Q J, Ghosh J, Yang Q, Motoda H, McLachlan G J, Ng A, Liu B, Yu P S, Zhou Z H H, Steinbach M, Hand D J and Steinberg D 2008 *Knowledge and Information Systems* **14** 1–37 ISSN 0219-3116 URL https://doi.org/10.1007/s10115-007-0114-2